Tuning APTES Silanization Window in PLA/Cellulose Nanofiber Biocomposites: Optimizing Interfacial Adhesion, Mechanical Strength, and Thermal Stability

Ramtin Ghorbanpour, Seyed Eshagh Ebadi,* Valiullah Moosavi, Mojtaba Soltani, and Mohsen Saffari

Polylactic acid (PLA) is limited by inherent brittleness and poor thermal stability, hindering its engineering applications. This study systematically investigated cellulose nanofibers (CNFs) silanized with 3- aminopropyl-triethoxysilane (APTES) at mass ratios of 2:1 (R5) and 4:1 (R7), incorporated into PLA at 0.5 wt% to 1.5 wt% levels. Unmodified 1.0 wt% CNFs (R2) enhanced impact strength (10.15 ± 0.50 kJ·m^{-2}) *via* pull-out toughening. Moderate silanization (R5) improved interfacial adhesion, achieving balanced tensile strength (50.2 ± 1.4 MPa), modulus (321 ± 16 MPa), and elongation (5.0 ± 0.2%). Stronger silanization (R7) increased modulus (545 ± 26 MPa) but reduced elongation (4.04 ± 0.18%), inducing brittleness. Fourier transform infrared analysis confirmed reduced hydroxyl groups and Si–O–Si/Si–O–C bond formations. Uniform interphases were observed in R5, while R7 exhibited voids and heterogeneity in scanning electron microscopy. Thermogravimetric analysis revealed higher onset (T_{onset} 352 ± 2 °C) and maximum decomposition (T_{max} 360 ± 2 °C) temperatures for R5 compared to R2 (335 ± 2 °C, 342 ± 2 °C). This study validates an "optimized silanization window" (2:1 ratio), enabling simultaneous enhancements in stiffness, toughness, and thermal stability for sustainable PLA/ CNFs biocomposites, suitable for industrially compostable packaging and biomedical applications.

DOI: 10.15376/biores.21.1.1172-1191

Keywords: PLA biocomposites; Cellulose nanofibers (CNFs); APTES silanization; Interphase engineering; Mechanical properties; Thermal stability; Fracture micromechanics; Optimized silanization window

Contact information: Department of Wood and Paper Science and Technology, Cha.C., Islamic Azad University, Chalus, Iran;
** Corresponding author: eshaghebadi@iau.ac.ir*

INTRODUCTION

The growing global demand for sustainable and eco-friendly materials has drawn considerable attention to bio-based and biodegradable polymers. Among them, poly(lactic acid) (PLA) is recognized as a key candidate for applications such as industrially compostable packaging, medical devices, and lightweight structures, owing to its renewable origin, degradability under industrial composting conditions, and favorable mechanical strength (Yang *et al*. 2020). These attributes align well with the United Nations' Sustainable Development Goal 12 on responsible consumption and production. However, the inherent brittleness, low elongation at break, and limited thermal stability of PLA restrict its engineering applications (Mandal *et al*. 2021). Therefore, the simultaneous improvement of strength, toughness, and thermal stability of PLA—without compromising its intrinsic properties—remains both a scientific and industrial necessity.

To enhance PLA performance, several strategies have been developed, including blending with flexible polymers (Wang *et al.* 2022), incorporation of bio-based plasticizers (Srisawat *et al*. 2022), and the addition of inorganic nanoparticles such as SiO_2 or ZnO (Kaseem 2021). The authors' previous study also demonstrated that graphene nanosheets could significantly improve the elastic modulus and tensile strength of PLA/beech-wood flour composites (Ghorbanpour *et al*. 2022). Despite these advances, challenges such as modulus reduction or loss of biodegradability remain. Consequently, the use of natural nanofillers such as CNFs has emerged as an effective approach due to their biocompatibility and ability to enhance both mechanical and thermal performance.

CNFs are considered ideal reinforcements for PLA because of their high specific modulus, low density, and efficient derivation from naturally abundant cellulose (Shi *et al*. 2025; Abdul Khalil *et al.* 2020). Uniform dispersion of CNFs within the PLA matrix facilitates effective stress transfer across the interphase and activates fracture mechanisms such as fiber pull-out and crack deflection (Nazrin *et al*. 2021). Nevertheless, the intrinsic incompatibility between hydrophilic CNFs and hydrophobic PLA often leads to fiber agglomeration and weak interfacial adhesion (Mandal *et al*. 2021). Surface modification of CNFs with the silane coupling agent 3-aminopropyl-triethoxysilane (APTES) can overcome this limitation. The coupling agent APTES reacts with hydroxyl groups on CNFs and ester groups in PLA, forming stable Si–O–Si and Si–O–C linkages, while its amino groups promote stronger interfacial compatibility (Magee *et al*. 2023; Zhang *et al*. 2023). The amino groups of APTES play a specific role in polar PLA matrices by forming hydrogen bonds with PLA carbonyl groups (NH_2 … O=C) and potentially enabling nucleophilic interactions during melt processing (Li *et al.* 2020; Panaitescu *et al.* 2022). While non-amino silanes (*e.g*., vinyl or alkyl) are effective in non-polar polymers (PP, PE) *via* hydrophobic matching, they exhibit weaker adhesion to polar PLA (Zhang *et al.* 2023). Thus, APTES was selected for its enhanced interfacial compatibility with PLA's chemistry.

Recent studies have confirmed that silanization improves the mechanical and thermal stability of PLA/CNFs composites (Liu *et al*. 2022; Yang *et al*. 2020). However, the effect of silanization intensity has received limited attention (Srisawat *et al*. 2022; Zhang *et al*. 2025). Insufficient silanization leaves unreacted hydroxyl groups, restricting adhesion, whereas excessive silanization produces heterogeneous layers that cause stress concentration and brittle fracture (Varghese *et al*. 2023). This contrast highlights the existence of an "optimized silanization window," which has seldom been systematically examined.

This study systematically defines and investigates the concept of an optimized silanization window in PLA/CNFs nanocomposites. Unlike previous works that primarily compared silanized and unsilanized systems (Qian *et al*. 2018; Liu *et al*. 2022; Lozano Fernandez and Miskolczi 2022), the present work analyzes the intensity of surface modification as a critical variable. The findings demonstrate that balanced interfacial adhesion, mechanical strength, and thermal stability are achieved only within a moderate silanization range-identified herein as the optimized silanization window.

The selection of APTES is further justified by its established biocompatibility and suitability for bio-based systems. The aminopropyl functionality is non-toxic at low concentrations and has been widely employed in biomedical coatings, drug delivery systems, and tissue-engineering scaffolds owing to its ability to promote cell adhesion and protein immobilization without inducing adverse immune responses (Panaitescu *et al.* 2022). In contrast to halogenated or mercapto-silanes, APTES does not generate cytotoxic

byproducts, making it a preferred coupling agent for sustainable and health-related applications of PLA/CNF composites (Goddard and Hotchkiss 2007)

MATERIALS AND METHODS

Materials

The main materials used in this study included PLA as the polymer matrix, CNFs as the reinforcing agent (either unmodified or surface-modified), and APTES as the surface coupling agent. Auxiliary solvents included ethanol and acetic acid (Table 1). APTES was selected due to its relative biocompatibility for bio-based applications (Li *et al*. 2020; Panaitescu *et al*. 2022).

Table 1. Materials Used in this Study

Material	Key Properties	Purity / Grade	Supplier
PLA	Density 1.30 g/cm³; T_m 170 to 180 °C; MFI 5 to 9 g/10min; T_g 60 to 63 °C	Injection grade	Nature Works (USA)
CNFs	2 wt% aqueous suspension; fibril diameter 30 to 50 nm	Mechanical grade	Domestic supplier
APTES	3-amino-propyltriethoxysilane	≥99%	Merck (Germany)
Ethanol	Solvent	96%, extra pure	Merck (Germany)
Acetic acid	pH adjustment	Glacial	Merck (Germany)

Surface Modification of Cellulose Nanofibers (CNFs)

Surface modification of CNFs with APTES was performed following the procedure reported by Shi *et al*. (2022), with two different silanization intensities. In the mild treatment (M1-CNF), a silane-to-cellulose mass ratio of 2:1 was used in an ethanol/water medium (pH 4.0, adjusted with 1% acetic acid) at 25 °C under magnetic stirring (300 rpm) for 24 h. In the intense treatment (M2-CNF), the same conditions were applied using a silane-to-cellulose ratio of 4:1. The modified products were centrifuged (8000 rpm, 5 min), washed three times with deionized water, and freeze-dried at −50 °C for 48 h to prevent agglomeration (Dong *et al.* 2014; Meng *et al*. 2022). To examine the effects of silanization intensity and CNFs loading, ten formulations (R0 to R9) were designed (Table 2).

Table 2. Compositions of PLA/CNFs Nanocomposite Samples (R0 to R9)

Sample Code	Matrix (wt%)	Reinforcement Type	Reinforcement Content (wt%)
R0	PLA (100)	–	–
R1	PLA (100)	CNF (Unmodified)	0.5
R2	PLA (100)	CNF (Unmodified)	1.0
R3	PLA (100)	CNF (Unmodified)	1.5
R4	PLA (100)	M1-CNF	0.5
R5	PLA (100)	M1-CNF	1.0
R6	PLA (100)	M1-CNF	1.5
R7	PLA (100)	M2-CNF	0.5
R8	PLA (100)	M2-CNF	1.0
R9	PLA (100)	M2-CNF	1.5

Preparation of Nanocomposites

Unmodified and APTES-modified CNFs (2:1 for M1 and 4:1 for M2) were incorporated into PLA at loading levels of 0.5 wt% to 1.5 wt%. Silanization was conducted in an ethanol/water medium under acidic conditions with magnetic stirring (Piorkowska *et al*. 2022). The PLA/CNFs nanocomposites were processed using a laboratory twin-screw extruder at 190 °C, 150 rpm, with a residence time of 8 min. The extruded strands were subsequently hot-pressed at 180 °C and 5 MPa to form composite sheets (Zhang *et al*. 2021; Shi *et al*. 2022).

Mechanical Testing

Tensile tests were conducted according to ASTM D638 on dumbbell-shaped specimens (gauge length 50 mm, crosshead speed 5 mm/min) with four replicates (n = 4) (Zhang *et al*. 2023). Izod impact tests were carried out on notched specimens following ASTM D256 (2014b). All data were reported as mean ± standard deviation and statistically analyzed using one-way ANOVA followed by Duncan's multiple range test ($P < 0.05$) (Srisawat *et al*. 2022).

Chemical and Thermal Analysis

Samples R2, R5, and R7 were selected for Fourier transform infra-red (FTIR), thermogravimetric analysis (TGA), and scanning electron microscopy with energy dispersive X-ray spectrometric (SEM/EDX) analyses, since the properties of neat PLA have been previously reported (Yang *et al*. 2020). FTIR spectra were obtained using a Bruker Tensor spectrometer (Germany) in the range of 400 to 4000 cm^{-1} with a resolution of 4 cm^{-1} (Gitari *et al*. 2019). TGA was carried out on a Mettler Toledo instrument (Switzerland) under nitrogen atmosphere at a heating rate of 10 °C/min from 25 to 600 °C, using approximately 5 mg of each sample (Yun *et al*. 2023). The SEM/EDX analyses were performed using a SNE-4500M microscope (Korea) on gold-coated specimens to examine fracture morphology and confirm the presence of Si and N elements. A summary of instruments used for processing and characterization is provided in Table 3.

Table 3. Instruments Employed for Processing and Characterization

Instrument	Model	Key Specifications
Cryogenic mill	Retsch ZM200	Mesh 40 sieve
Laboratory Single-Screw Extruder	HMI, Delta	190 °C; 150 rpm
Hot press / Cold press	Hydraulic press	180 °C; 5 bar; 5 min
FTIR	Bruker Tensor	400 to 4000 cm^{-1}; resolution 4 cm^{-1}
TGA	Mettler Toledo	25 to 600 °C; 10 °C/min; 5 mg sample
SEM/EDX	SNE-4500M	10 to 15 kV; gold coating
Tensile tester	Universal testing machine	ASTM D638; 5 mm/min; gauge length 50 mm
Impact tester	Izod impact tester	ASTM D256; notched samples

RESULTS AND DISCUSSION

Tensile and Impact Tests

Tensile and impact tests were conducted to evaluate the effects of CNFs and surface modification with APTES on the performance of PLA-based biocomposites. The data were expressed as mean ± standard deviation (four replicates) and statistically analyzed using

one-way ANOVA followed by Duncan's multiple range test (α = 0.05). The results are presented in Figs. 1–4.

Tensile Strength

Neat PLA (R0) exhibited a tensile strength of 46.6 ± 2.0 MPa, showing a typical brittle behavior. The incorporation of unmodified CNFs (R1–R3) enhanced the tensile strength; the R2 sample (1 wt% CNFs) achieved the highest improvement (50.2 ± 1.4 MPa), which was statistically different from neat PLA. At a higher CNFs loading (R3), the strength further increased to 55.5 ± 2.6 MPa, though variations were observed in other mechanical properties. Mild surface modification (M1-CNF, APTES-to-cellulose ratio 2:1) in samples R4–R6 improved fiber–matrix compatibility. The sample R5 (1 wt% M1-CNF) exhibited a tensile strength between 49 and 52 MPa, which was statistically distinct from that of unmodified CNFs composites. In contrast, severe modification (M2-CNF, ratio 4:1) in R7 to R9 led to a substantial decrease in tensile strength (R7: 24.3 ± 0.5 MPa). This reduction is attributed to the formation of thick and heterogeneous silane layers, which caused stress concentration and brittle fracture (Feng *et al*. 2020) (Fig. 1).

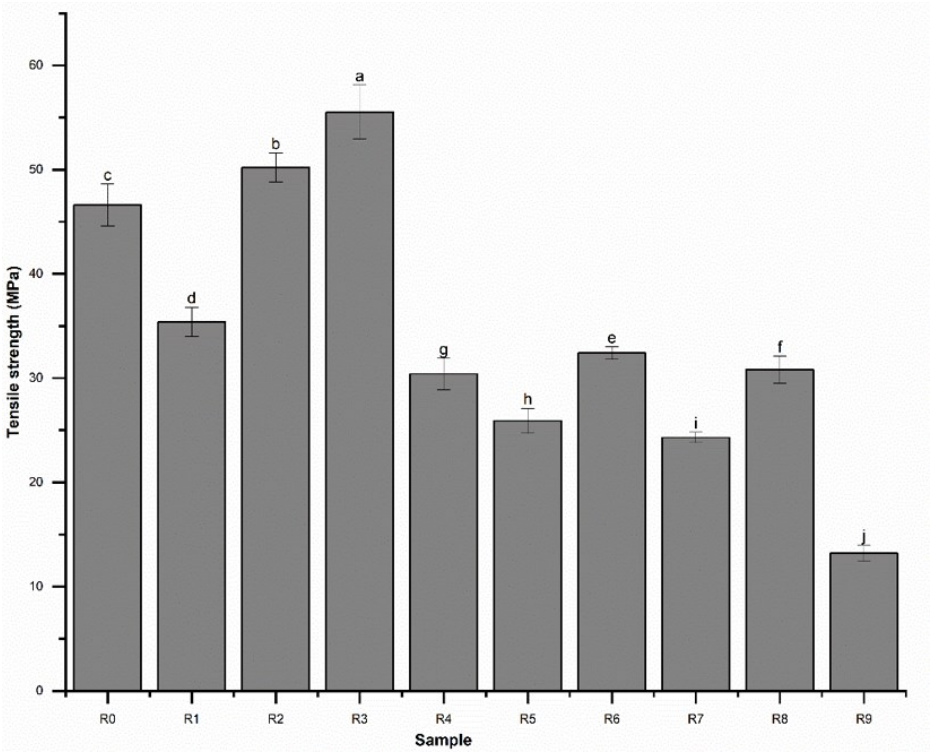

Fig. 1. Tensile strength (mean ± SD, n = 4) of PLA/CNF composites (R0 to R9) with Duncan's grouping (letters above bars, α = 0.05). Specimen codes: R0 = neat PLA; R1 to R3 = unmodified CNF (0.5 to 1.5 wt%); R4 to R6 = M1-CNF (APTES:cellulose = 2:1, 0.5 to 1.5 wt%); R7 to R9 = M2-CNF (APTES:cellulose = 4:1, 0.5 to 1.5 wt%).

Elastic Modulus

The tensile modulus results are shown in Fig. 2. Neat PLA exhibited a modulus of 293 ± 13 MPa. The addition of unmodified CNFs (R1–R3) had a limited effect, with the R2 sample showing a modulus of 261 ± 17 MPa, indicating unstable reinforcement due to the absence of strong chemical bonding (Lu *et al*. 2022). In contrast, mild surface modification (M1-CNF, 2:1 APTES-to-cellulose ratio) in R5 increased the modulus to 321

± 16 MPa, suggesting effective stress transfer at the interfacial region owing to the formation of silanol linkages and Si–O–Si networks (Yang *et al*. 2020). Severe modification (M2-CNF, 4:1 ratio) in R7 resulted in a modulus of 545 ± 26 MPa, nearly twice that of neat PLA. However, this increase in stiffness was accompanied by a significant loss of toughness, indicating excessive interphase hardening.

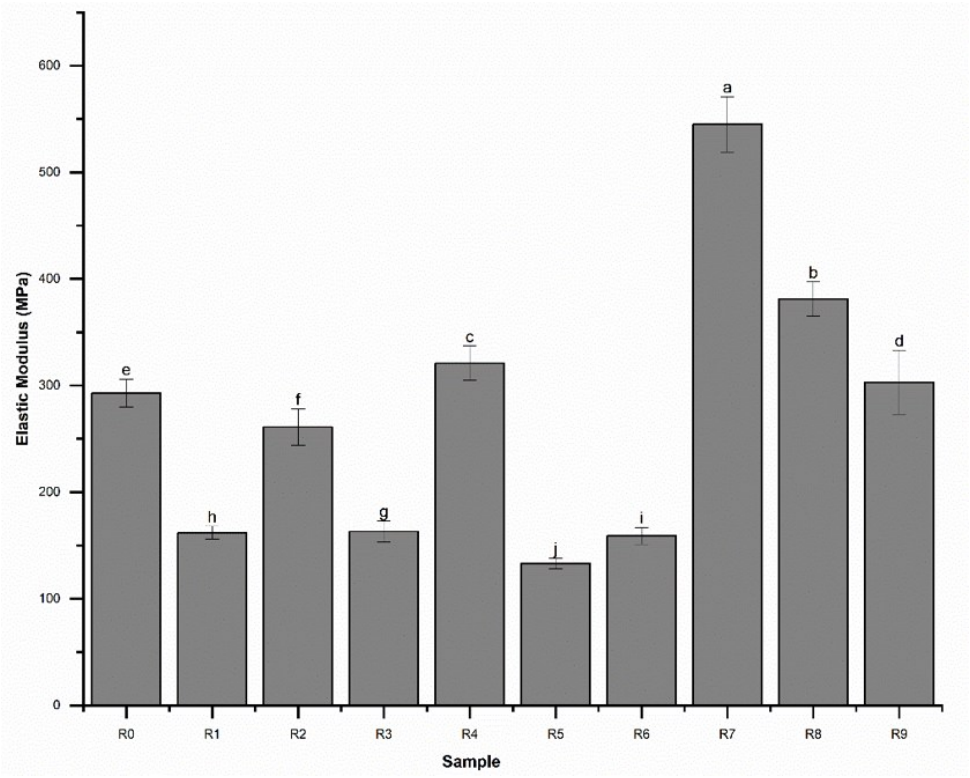

Fig. 2. Elastic modulus (mean ± SD, n = 4) of PLA/CNFs composites (R0–R9) with Duncan's grouping (letters above bars, α = 0.05)

Elongation at Break

Elongation at break, as an indicator of flexibility, is presented in Fig. 3. Neat PLA exhibited an elongation at break of 7.25% ± 0.93%. The addition of unmodified CNFs slightly increased the elongation, reaching 9.18% ± 0.77% for R3. This improvement is attributed to fiber pull-out and microcrack deflection mechanisms (Khan *et al*. 2021). In the M1-CNF group (2:1 APTES-to-cellulose ratio), the elongation decreased to 5.25% ± 0.62% in R5, likely due to restricted polymer chain mobility caused by stronger interfacial bonding. In the M2-CNF group (4:1 ratio), this reduction was more pronounced, with R7 showing only 4.04% ± 0.18%, indicating a loss of flexibility resulting from excessive interphase stiffness.

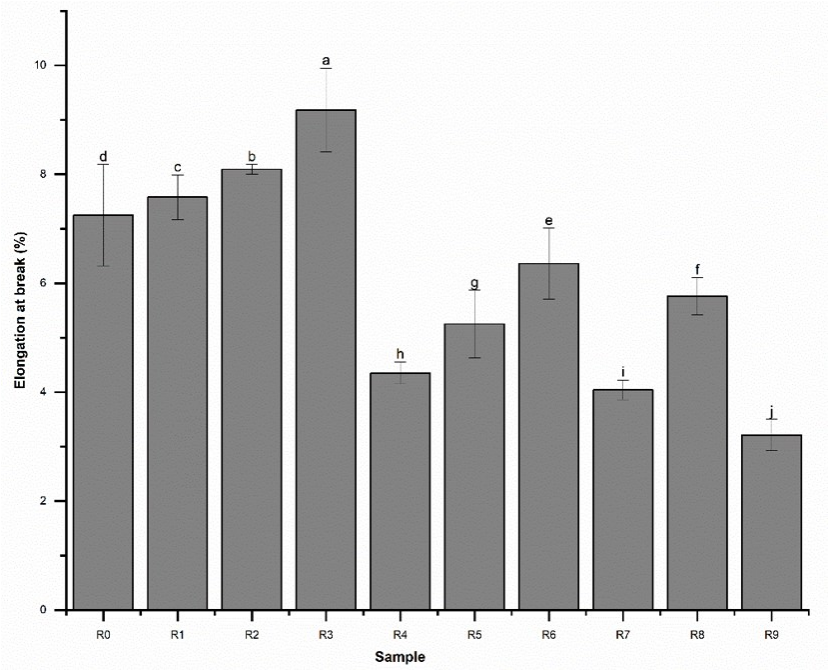

Fig. 3. Elongation at break (mean ± SD, n = 4) of PLA/CNFs composites (R0 to R9) with Duncan's grouping (letters above bars, α = 0.05)

Impact Strength

Impact strength, an indicator of toughness, is shown in Fig. 4. Neat PLA exhibited a low impact resistance of 3.59 ± 0.23 kJ/m². In the unmodified CNFs group, sample R2 achieved the highest improvement (10.15 ± 0.50 kJ/m²), which was nearly three times that of neat PLA.

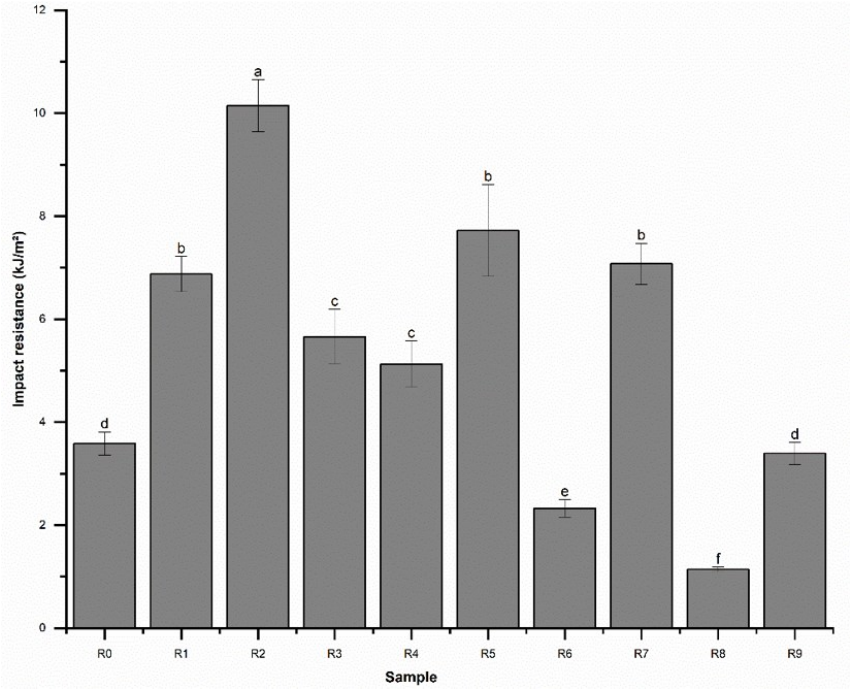

Fig. 4. Impact resistance (mean ± SD, n = 4) of PLA/CNFs composites (R0 to R9) with Duncan's grouping (letters above bars, α = 0.05)

This enhancement is attributed to fiber pull-out and crack deflection mechanisms. In the M1-CNF group (2:1 APTES-to-cellulose ratio), sample R5 recorded an impact strength of 7.72 ± 0.89 kJ/m², which, although lower than R2, provided a balanced combination of strength and toughness along with increased stiffness. In the M2-CNF group (4:1 ratio), impact resistance decreased; particularly, R9 showed 1.14 ± 0.05 kJ/m² and R7 7.08 ± 0.40 kJ/m², indicating that the system's toughness was highly sensitive to the intensity of surface modification.

Mechanical tests revealed that the quality of the interfacial region was the key factor governing the performance of PLA/CNFs composites. In sample R2 (PLA + 1 wt% unmodified CNFs), weak interfacial adhesion promoted reinforcement through a fiber pull-out mechanism, leading to an increase in impact strength to 10.15 ± 0.50 kJ/m². In R5 (PLA + 1 wt% M1-CNF), improved interfacial bonding enhanced both tensile strength and modulus to 50.2 ± 1.4 MPa and 321 ± 16 MPa, respectively, achieving a desirable balance between stiffness and toughness. Conversely, R7 (PLA + 0.5 wt% M2-CNF) exhibited a higher modulus (545 ± 26 MPa) but lower elongation at break (4.04 ± 0.18%) and impact strength (7.08 ± 0.40 kJ/m²), indicating a more brittle behavior caused by excessive surface modification.

Based on Figs. 1 to 4 and Table 3, R2, R5, and R7 were selected as representative samples for unmodified, mildly modified, and heavily modified CNFs composites, respectively. These samples were subjected to FTIR, TGA, and SEM/EDX analyses to further elucidate the relationship between interfacial structure and mechanical performance.

Pearson correlation analysis was performed on the mean mechanical properties (Table 4). A strong negative correlation was observed between the elastic modulus and elongation at break ($r = -0.872$, $p < 0.001$), which was attributed to over-silanization effects in samples R7 to R9. When these formulations were excluded, strong positive correlations emerged among tensile strength, elongation, and impact strength ($r = 0.76–0.92$), confirming the synergistic reinforcement and optimized interfacial bonding achieved under moderate silanization conditions (*e.g.*, R5). This statistical analysis supports the structure–property relationships discussed earlier.

Table 4. Pearson Correlation Coefficients (r) between Mean Mechanical Properties of PLA/CNF Composites (n = 10 formulations)

Property	Tensile Strength	Elastic Modulus	Elongation at Break	Impact Strength
Tensile Strength	1.000	–0.485	0.312	0.210
Elastic Modulus	–0.485	1.000	**–0.872**	–0.315
Elongation at Break	0.312	**–0.872**	1.000	0.428
Impact Strength	0.210	–0.315	0.428	1.000

Note: Bold values indicate strong correlations (|r| > 0.7). ** p < 0.01; * p < 0.05. Values were computed using mean data extracted from Figs. 1 to 4.

FTIR Analysis

To examine interfacial chemical changes and confirm the surface modification of CNFs, FTIR analysis was performed on samples R2 (PLA + 1 wt% unmodified CNFs), R5 (PLA + 1 wt% M1-CNF, APTES ratio 2:1), and R7 (PLA + 0.5 wt% M2-CNF, APTES ratio 4:1). The normalized FTIR spectra are presented in Fig. 5.

All FTIR spectra were normalized to the PLA carbonyl (C=O) stretching peak at ~1750 cm^{-1} to account for minor differences in CNF loading and ensure that band intensity variations reflect silanization degree, not filler content (Fortunati *et al.* 2012; Shi *et al.* 2022).

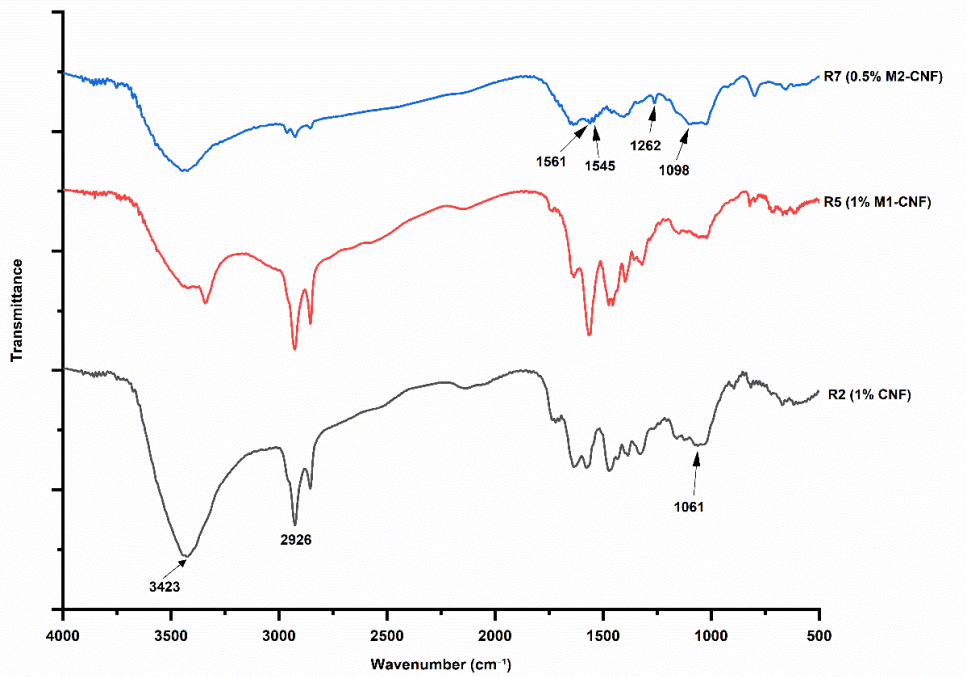

Fig. 5. Normalized FTIR spectra of PLA/CNFs composites: R2 (PLA + unmodified CNFs), R5 (PLA + M1-CNF, silanized with APTES at a 2:1 ratio), and R7 (PLA + M2-CNF, silanized with APTES at a 4:1 ratio). Key absorption bands are annotated.

Normalized FTIR spectra of R2, R5, and R7 in the range of 400 to 4000 cm^{-1} were analyzed to assess structural variations induced by CNFs surface modification. A broad band in the 3200 to 3500 cm^{-1} region, corresponding to O–H stretching vibrations, was observed in all samples. The higher intensity of this band in R7 indicates an increase in polar groups or altered hydrogen bonding interactions as a result of APTES treatment (Hongyu *et al*. 2024). The peaks near 2900 cm^{-1} (–CH_2 and –CH_3 stretchings) and 1735 to 1750 cm^{-1} (C=O stretching) confirm the stability of the PLA backbone across all samples (Fortunati *et al*. 2012; Moscoso *et al*. 2019). In R5 and particularly in R7, new bands appeared in the 1500 to 1600 cm^{-1} region, corresponding to N–H bending vibrations, confirming the covalent bonding of APTES amino groups to CNFs—absent in R2 (Tee *et al*. 2013). The bands at 1000 to 1100 cm^{-1}, attributed to Si–O–Si and Si–O–C stretching, emerged in the modified samples with greater intensity in R7, suggesting higher silanization efficiency at the 4:1 ratio (Li *et al*. 2014; Yang *et al*. 2017). The 1080 to 1180 cm^{-1} region (C–O–C stretching of PLA) overlapped with the silane-related bands, requiring complementary analysis for precise interpretation (Plackett *et al*. 2010). R7 (0.5 wt% M2-CNF) was selected, as it exhibited the highest stiffness and lowest toughness among the intense silanization group (4:1 APTES ratio), representing the critical over-silanization condition. Normalized spectra and comparison with R8 (1.0 wt%) confirmed that Si–O–Si intensity increased with APTES ratio, independent of CNF loading. In summary, the appearance of Si–O–Si, Si–O–C, and N–H bands in R5 and R7—particularly their stronger intensity in R7—confirmed the successful chemical modification of CNFs. These spectral changes facilitate improved interfacial adhesion and are expected to enhance the

mechanical integrity and structural homogeneity of the composites, consistent with previous studies (Suryanegara *et al*. 2010; Mohammed *et al*. 2022).

SEM Analysis

To elucidate the interfacial micromechanisms underlying the mechanical behavior (strength, modulus, elongation, and impact) and the FTIR observations, the surface and fracture morphologies were examined using SEM, while elemental content was obtained from EDX analysis. The objective was to establish a direct correlation between the intensity of APTES silanization, the interphase architecture, and the fracture pattern, in order to explain the observed "stiffness enhancement *versus* toughness reduction" at different silane loadings. SEM observations focused on R5 (mild silanization, 2:1 ratio) and R7 (intense silanization, 4:1 ratio), since R5 exhibited a balanced interphase and R7 demonstrated a high modulus but increased brittleness. Sample R2 (unmodified CNFs) had been previously characterized, and the morphology of untreated CNFs within the PLA matrix has been well documented; thus, the emphasis here was placed on silanized samples to assess the effect of coating intensity (Kamran *et al*. 2022).

Surface morphology

At low magnifications (100× and 300×), R5 displayed a smoother surface with a more homogeneous dispersion of the reinforcing phase (Figs. 6a, 6b).

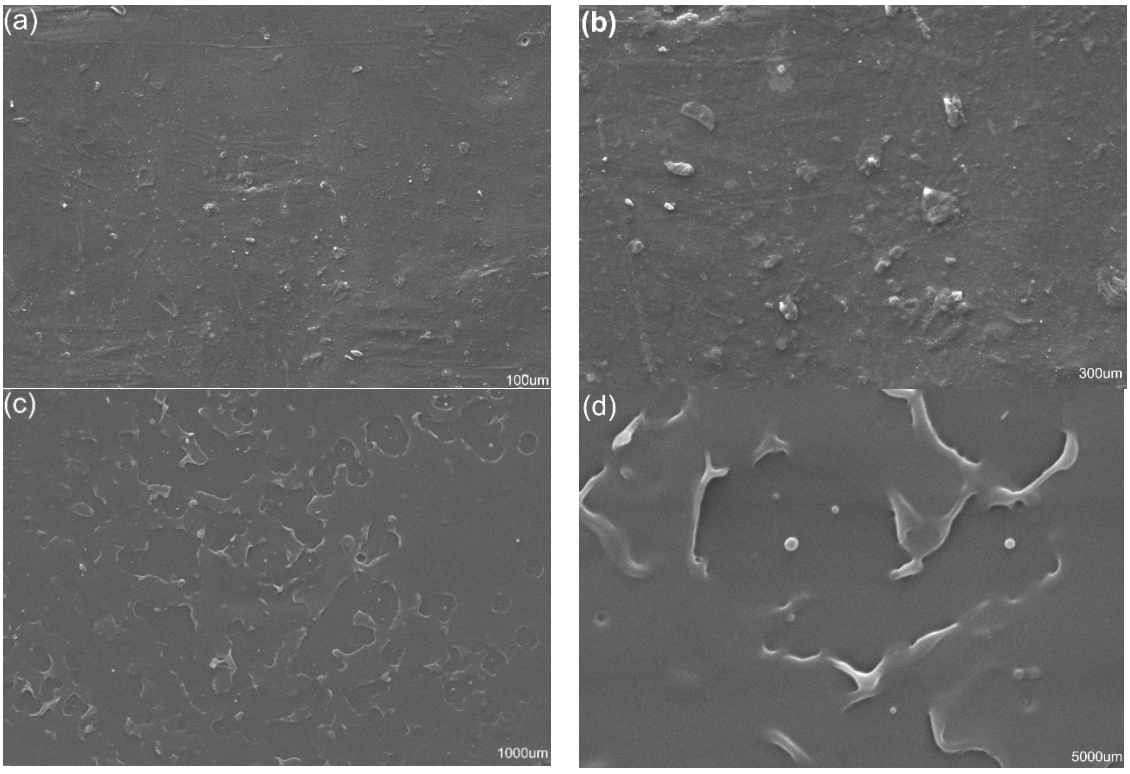

Fig. 6. SEM micrographs of sample R5 (PLA/M1-CNF, silane-to-cellulose ratio 2:1): (a) surface at 100×, (b) surface at 300×, (c) fracture surface at 1000×, and (d) fracture surface at 5000×. These images reveal relatively uniform dispersion of CNFs

Traces of flow-induced alignment were visible, but voids surrounding the fibrils were sparse and small—consistent with improved wettability and reduced surface energy

in the presence of a thin silane layer. These observations correspond well with FTIR results (reduced O–H band and appearance of Si–O–Si/Si–O–C vibrations), confirming the formation of chemical bridges and a decrease in interfacial porosity (Panaitescu *et al*. 2021).

In R7 (Figs. 7a, 7b), a greater presence of surface particles, patchy regions, and irregular microvoids was observed, indicating a thicker and more heterogeneous silane coating. This morphological pattern correlates well with the reduced elongation at break and impact strength, suggesting that excessive silanization led to a brittle interphase structure. In summary, R5 exhibited a cleaner surface with fewer voids, corresponding to better wettability and interfacial compatibility, whereas R7 showed a more spotted and porous morphology, consistent with the formation of a thicker and non-uniform silane layer.

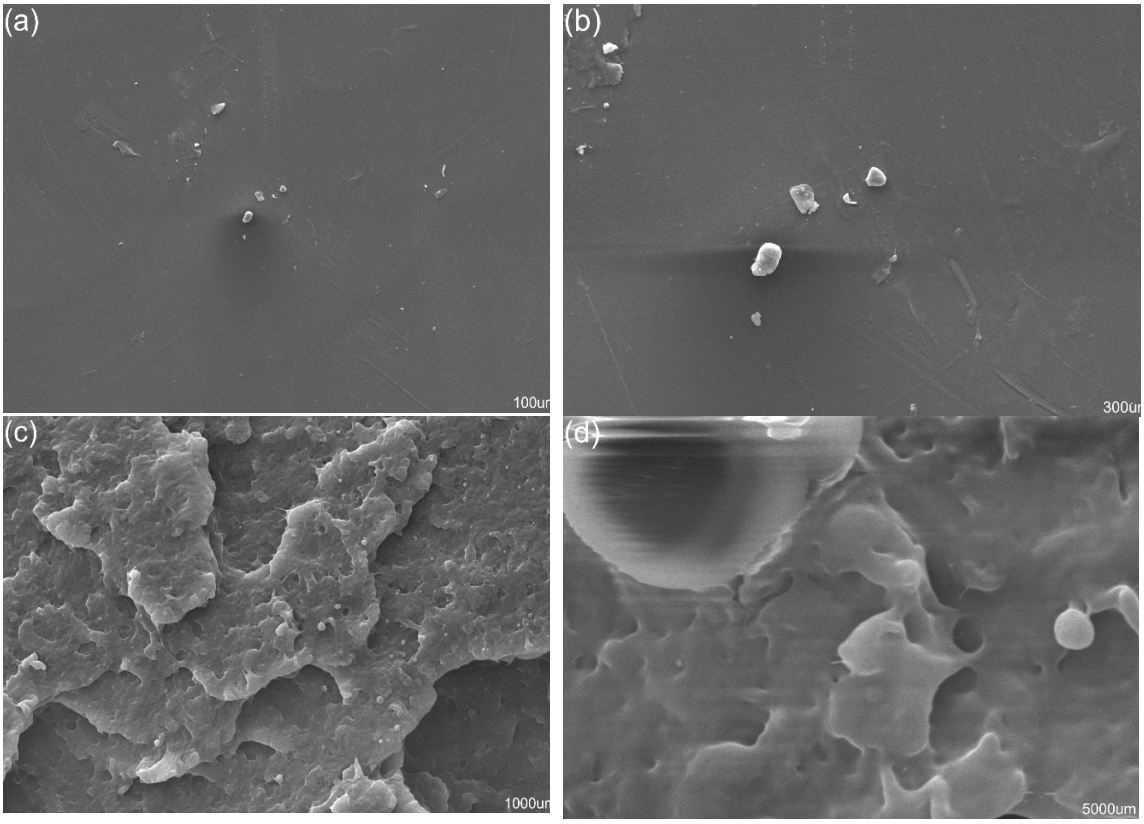

Fig. 7. SEM micrographs of sample R7 (PLA/M2-CNF, silane-to-cellulose ratio 4:1): (a) surface at 100×, (b) surface at 300×, (c) fracture surface at 1000×, and (d) fracture surface at 5000×. The images show fiber agglomeration, voids, and long pull-outs.

Fracture surface morphology

At higher magnifications (1000× and 5000×), distinct fracture patterns were observed. In R5 (Figs. 6c, 6d), shorter fiber pull-outs, plastic shear bands within the PLA matrix, and textured fracture surfaces were evident, consistent with the presence of Si–O–C and Si–O–Si chemical linkages that promote efficient stress transfer (Zhao *et al*. 2020). This morphology reflects higher modulus and strength combined with moderate toughness, as the shorter pull-out lengths and smaller voids indicate greater energy absorption through matrix shear deformation rather than interfacial debonding. In R7 (Figs. 7c, 7d), smoother, step-like fracture surfaces, extended interfacial cracks, and larger voids with a wider pull-

out length distribution were observed, indicating localized stress concentration and brittle failure. This fracture pattern aligns with the FTIR findings (stronger silane-related signals) and the mechanical results (higher modulus but lower elongation and impact strength), confirming the occurrence of excessive silanization (Ghasemi *et al*. 2022).

Micromechanical summary

The distribution of fiber pull-out lengths and the size and density of voids serve as key indicators of the balance between energy absorption and stress transfer. In R5, shorter pull-outs accompanied by shear bands and smaller voids signify efficient stress transfer and balanced reinforcement. In contrast, R7 exhibited cleaved surfaces with interfacial cracks and larger voids, reflecting stress concentration and brittle fracture behavior.

EDX Analysis

To verify the interfacial chemistry and distinguish the effect of APTES silanization intensity, EDX analysis was conducted on R2 (PLA + 1 wt% unmodified CNFs, non-silanized control) and R5 (PLA + 1 wt% M1-CNF, APTES-to-cellulose ratio 2:1, optimized interphase). This selection aimed to (i) identify the presence or absence of Si and N elements, (ii) avoid inaccurate quantitative comparison of silanization intensities due to the inherent limitations of EDX (matrix effects and interaction volume), and (iii) provide elemental evidence supporting the mechanical, FTIR, and SEM findings (Goldstein *et al*. 2022). The elemental weight percentages (wt%) are summarized in Table 5 and illustrated in Fig. 8.

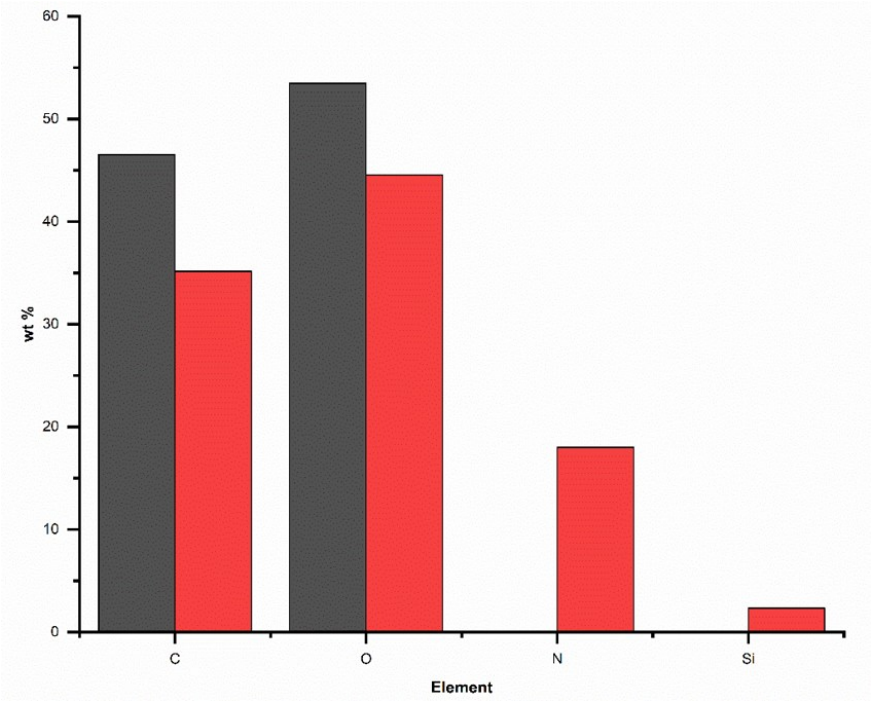

Fig. 8. Elemental composition (wt%) for R2 (C 46.53, O 53.47, N 0.00, Si 0.00) and R5 (C 35.16, O 44.54, N 17.98, Si 2.32) obtained from EDX analysis. Values are interpreted semi-quantitatively.

In R2, only carbon (C, 46.53 wt%) and oxygen (O, 53.47 wt%) were detected, consistent with the expected composition of the PLA/CNFs system without silane treatment. In R5, in addition to C (35.16 wt%) and O (44.54 wt%), N (17.98 wt%), and Si

(2.32 wt%) were identified, corresponding respectively to the amino groups and siloxane/siloxy linkages (Si–O–Si and Si–O–C) derived from APTES. These findings agree well with the FTIR results, which showed the reduction of the O–H band and the appearance of Si–O–Si/Si–O–C bands near 1000 to 1100 cm^{-1}, confirming the formation of a chemical interfacial layer in R5 (Kasprzhitskii *et al*. 2021).

Table 5. EDX Elemental Composition of R2 (Raw CNF) and R5 (M1-CNF, APTES 2:1)

Element	CNFs (wt%)	M1-CNF (wt%)
C	46.53	35.16
O	53.47	44.54
N	0.0	17.98
Si	0.0	2.32

The presence of Si and N contents in R5 is consistent with the SEM observations (improved wettability, fewer voids, and shorter fiber pull-outs in Figs. 6c–d) and the mechanical results (enhanced strength and modulus). This correlation confirms efficient stress transfer through chemical bonding at the interface. In contrast, the absence of Si and N in R2 corresponds to an interphase governed by hydrogen bonding and physical interactions, characterized by longer pull-outs, higher toughness, and limited modulus (Fig. 4). EDX analysis was not performed for R7 due to its limited explanatory value, considering the method's semi-quantitative nature and matrix effects. Moreover, FTIR and SEM results were sufficient to identify the heterogeneous and brittle coating (Chandrasekar *et al*. 2021). EDX confirmed the presence of Si and N in R5, indicating the formation of Si–O–Si/Si–O–C bridges and amino functional groups that established a continuous and efficient interphase, resulting in a balanced strength–toughness profile. Conversely, R7, based on FTIR and SEM findings, exhibited a thicker and non-uniform silane coating that led to stress concentration and brittle fracture. Although quantitative interpretation of EDX was performed with caution—owing to calibration limitations, light-element sensitivity, and ZAF corrections—the consistency between EDX, FTIR, and SEM data strongly supported the existence of an optimized interphase in R5 (Abdulkhalil *et al*. 2020; Yu *et al*. 2020). It is expected that this optimized interphase in R5 will result in higher T_{onset} and T_{max} values in the TGA analysis compared with R2, whereas the structural heterogeneity of R7 may yield a more complex thermal degradation behavior.

TGA

To evaluate the effect of APTES silanization intensity on the thermal stability of PLA/CNFs nanocomposites, TGA and derivative thermogravimetric (DTG) analyses were performed on R2 (PLA + 1 wt% unmodified CNFs), R5 (PLA + 1 wt% M1-CNF, APTES-to-cellulose ratio 2:1), and R7 (PLA + 0.5 wt% M2-CNF, ratio 4:1). The data for the onset degradation temperature (T_{onset}), maximum degradation temperature (T_{max}), and residual char at 600 °C and 750 °C are presented in Fig. 9 and Table 6.

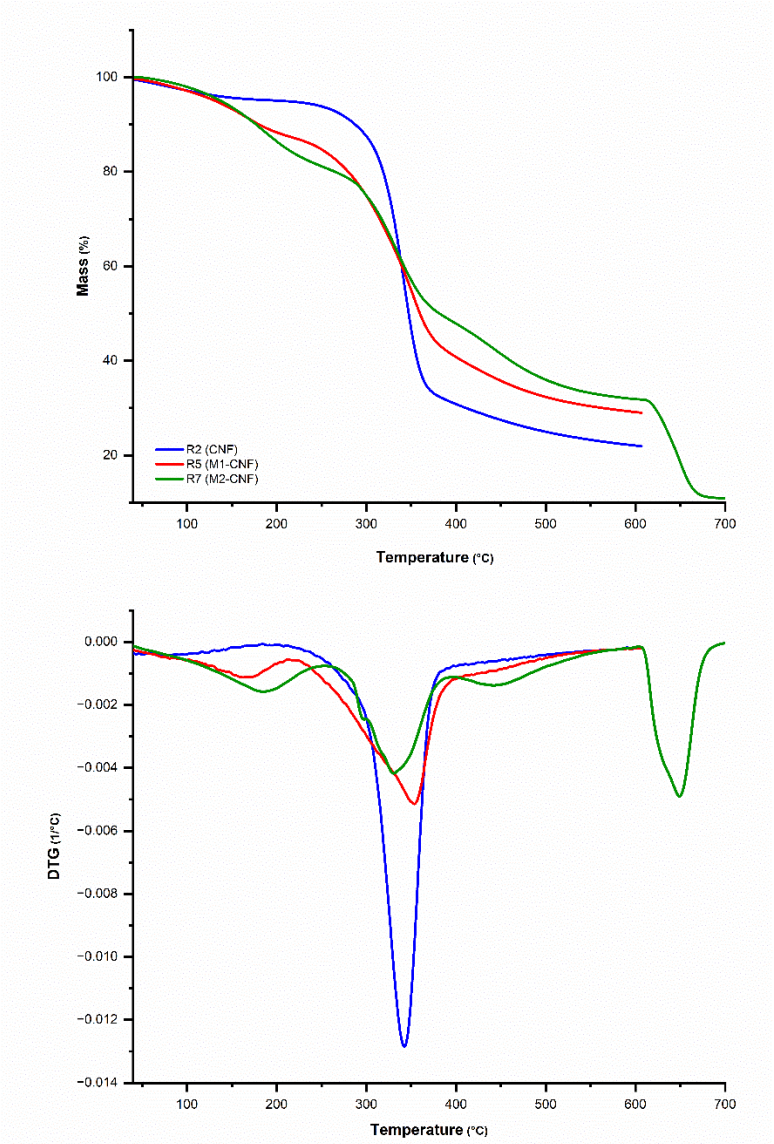

Fig. 9. TGA/DTG curves of CNFs samples: R2 (CNFs), R5 (M1-CNF, 2:1 APTES), and R7 (M2-CNF, 4:1 APTES).

Table 6. Thermal Degradation Parameters Obtained from TGA/DTG Curves for R2 (Raw CNF), R5 (M1-CNF, 2:1), and R7 (M2-CNF, 4:1)

Parameter	R2	R5	R7
Baseline mass (%)	99.08	99.29	99.74
T_{onset} (°C)	310	325	330
T_{max} (°C)	342.5	353.3	330.3
T_{50} (°C)	348.3	360.8	383.7
Residue 600 °C (%)	22.06	29.14	31.89
Residue 750 °C (%)	—	—	2.72

The TGA curves revealed that the incorporation of CNFs into PLA delayed the onset of thermal degradation and improved resistance to initial mass loss within the 300 to 380 °C range (Gitari *et al.* 2019). For R2, the T_{onset} and T_{max} values were approximately 310 °C and 342 °C, respectively. In R5 (mildly silanized sample), T_{onset} and T_{max} increased to

325 °C and 353 °C, respectively, attributed to the reduction of free –OH groups and the formation of stable Si–O–C and Si–O–Si linkages. The residual char at 600 °C increased from 22% (R2) to 29% (R5), consistent with the presence of a more thermally stable inorganic phase (Thomas *et al*. 2021). In R7 (intense silanization), T_{onset} reached 330 °C, while T_{max} decreased to 330 °C, indicating silane coating heterogeneity. The residual char of R7 (32%) was the highest, reflecting the increased inorganic content.

Effect of Mild Silanization (R5 – 2:1 Ratio)

In R5, the 15 to 20 °C increase in T_{onset} and T_{max} compared to R2 was due to the reduction of –OH groups and the formation of Si–O–Si and Si–O–C bonds, which delayed the onset of degradation. The amino groups in APTES also promoted hydrogen bonding with PLA, facilitating more uniform heat transfer. These findings align with FTIR (reduced O–H band and enhanced Si–O–Si peaks) and SEM/EDX results (presence of Si and N), confirming a dense and thermally stable interphase that correlates with higher tensile modulus and strength.

Effect of Intense Silanization (R7)

In R7, the slight increase in T_{onset} but decrease in T_{max} indicates over-silanization and coating heterogeneity, consistent with SEM observations (voids and agglomerates) and EDX evidence. Although the higher residual char (32%) reflects greater silane content, the coating heterogeneity led to lower structural uniformity and weaker mechanical properties.

Overall Observation

Mild silanization (R5) provided an optimal balance between thermal stability and structural integrity, while intense silanization (R7), despite a slight thermal improvement, caused deterioration in mechanical performance due to interfacial heterogeneity. The higher char yield observed in R5 and R7, relative to neat PLA (Fig. 9), is attributed to condensation reactions among transient silanol (Si–OH) and cellulosic hydroxyl (C–OH) groups occurring within the 150 to 300 °C range, leading to the formation of cross-linked Si–O–C and Si–O–Si networks that serve as thermally insulating barriers (Fox *et al.* 2013; Yu *et al.* 2018). These in-situ generated char precursors enhance flame retardancy by suppressing volatile release and promoting carbonaceous residue formation. This mechanism is consistent with the over-silanization behavior observed in R7, where excess APTES contributes to the development of a siloxane-rich char layer. These findings confirm the concept of an "optimized silanization window" and are in good agreement with the FTIR and SEM/EDX analyses.

CONCLUSIONS

1. Mild 3- aminopropyl-triethoxysilane (APTES) silanization (2:1 ratio, R5) improved the tensile strength (~50 MPa), modulus (~321 MPa), and thermal stability (T_{onset} ~325 °C, T_{max} ~353 °C) of poly(lactic acid)/cellulose nanofiber (PLA/CNFs) nanocomposites. The formation of a balanced interphase enhanced stress transfer while preserving toughness.

2. Unmodified CNFs (R2) increased the impact strength (~10.2 kJ·m^{-2}) through physical mechanisms such as fiber pull-out; however, due to weak interfacial adhesion, the improvement in modulus was limited.
3. Intense silanization (4:1 ratio, R7) significantly increased the modulus (>545 MPa) but reduced elongation (~4%) and impact strength (~7.08 kJ·m^{-2}), as the thick and heterogeneous silane layers led to stress concentration and brittle fracture.
4. Fourier transform infrared (FTIR), scanning electron microscope (SEM), and EDX analyses confirmed the formation of Si–O–Si and Si–O–C linkages and the reduction of –OH groups in R5, indicating a uniform chemical interphase, whereas R7 exhibited heterogeneity and void formation.
5. The concept of an "optimized silanization window" was verified, demonstrating that only moderate modification (2:1 ratio) simultaneously optimizes interfacial adhesion and mechanical performance, while promoting greater char formation that contributes to improved thermal degradation behavior, rather than intrinsic thermal stability, in PLA/CNF biocomposites.

ACKNOWLEDGMENTS

The authors would like to express their sincere gratitude to Islamic Azad University, Chalous Branch, for supporting this research study. Additional appreciation is extended to Tose'e Mohit Zist va Gostareshe Sanaye Choob Shomal Co. (Wood and Environmental Industries Development Company), Iran, for providing materials and technical assistance during the experimental work.

Conflict of Interest

The authors declare that there are no conflicts of interest that could have influenced the research or publication of this manuscript.

Use of Generative AI

The authors used ChatGPT (OpenAI, USA) solely for English language editing. The content, data, and scientific interpretation were fully produced and verified by the authors.

REFERENCES CITED

Abdul Khalil, H. P. S., Adnan, A. S., Yahya, E. B., Olaiya, N. G., Safrida, S., Hossain, M. S., Balakrishnan, V., Gopakumar, D. A., Pasupathy, C. P., Oyekanmi, A. A., and Oyenero, O. D. (2020). "A review on plant cellulose nanofiber-based aerogels for biomedical applications," *Polymers* 12(8), article 1759. https://doi.org/10.3390/polym12081759

ASTM D256-10 (2014). "Standard test methods for determining the Izod pendulum impact resistance of plastics," ASTM International, West Conshohocken, PA.

ASTM D638-14 (2014). "Standard test method for tensile properties of plastics," ASTM International, West Conshohocken, PA.

Dong, J., Li, M., Zhou, L., Lee, S., and Yuan, C. (2014). "Comparison of 3-aminopropyltriethoxysilane (APTES) grafted on silica nanoparticles and APTES grafted after acid silica treatment on carbon dioxide adsorption," *Journal of Material Sciences and Engineering* 6(2), article 1000321. https://doi.org/10.4172/2169-0022.1000321

Fox, D. M., Lee, J., Citro, C., and Novy, M. (2013). "Flame retarded poly(lactic acid) using POSS-modified cellulose. 1. Thermal and combustion properties of intumescing composites," *Polymer Degradation and Stability* 98(1), 6-14. https://doi.org/10.1016/j.polymdegradstab.2012.11.016

Fortunati, E., Puglia, D., Monti, M., Santulli, C., Maniruzzaman, M., and Kenny, J. M. (2012). "Cellulose nanocrystals extracted from okra fibers in PVA nanocomposites," *Carbohydrate Polymers* 87(2), 1596-1605. https://doi.org/10.1002/app.38524

Goddard, J. M., and Hotchkiss, J. H. (2007). "Polymer surface modification for the attachment of bioactive compounds," *Progress in Polymer Science* 32(7), 698-725. https://doi.org/10.1016/j.progpolymsci.2007.04.002

Ghasemi, S., Tajvidi, M., Gardner, D. J., and Bousfield, D. W. (2022). "Interfacial shear strength of silane-treated cellulosic fibers in PLA studied by single fiber pull-out," *International Journal of Adhesion and Adhesives* 112, article 103014. https://doi.org/10.1016/j.ijadhadh.2021.103014

Ghorbanpour, R., Ghasemi, I., and Naeimian, N. (2022). "Investigation of the effect of graphene nanosheets on the properties of beech/polylactic acid flour composites," *Journal of Thermoplastic Composite Materials* 36(6), article 08927057221103413. https://doi.org/10.1177/08927057221103413

Gitari, B., Chang, B. P., Misra, M., Navabi, A., and Mohanty, A. K. (2019). "A comparative study on the mechanical, thermal, and water barrier properties of PLA nanocomposite films prepared with bacterial nanocellulose and cellulose nanofibrils," *BioResources* 14(1), 1867-1889. https://doi.org/10.15376/biores.14.1.1867-1889

Goldstein, J. I., Newbury, D. E., Joy, D. C., Lyman, C. E., Echlin, P., Lifshin, E., Sawyer, L., and Michael, J. R. (2022). *Scanning Electron Microscopy and X-ray Microanalysis*, 5th Ed., Springer. https://doi.org/10.1007/978-3-030-96393-7

Kamran, M. J., Jayamani, E., Heng, S. K., Wong, Y. C., Rahman, M. R., Al-Bogami, A. S., Huda, D., Bin Bakri, M. K., and Rahman, M. M. (2022). "Characterization and comparative study on chemically treated luffa fiber as reinforcement for polylactic acid bio-composites," *BioResources* 17(2), 2576-2597. https://doi.org/10.15376/biores.17.2.2576-2597

Kaseem, M., Ur Rehman, Z., Hossain, S., Singh, A. K., and Dikici, B. (2021). "A review on synthesis, properties, and applications of polylactic acid/silica composites," *Polymers* 13(18), article 3036. https://doi.org/10.3390/polym13183036

Kasprzhitskii, A., Lazorenko, G., Kruglikov, A., Kuchkina, I., and Gorodov, V. (2021). "Effect of silane functionalization on properties of poly(lactic acid)/palygorskite nanocomposites," *Inorganics* 9(1), article 3. https://doi.org/10.3390/inorganics9010003

Li, Y., Hu, C., and Yu, Y. (2020). "Enhanced interface and mechanical properties of PLA/cellulose nanofiber biocomposites via silane coupling," *Polymer Composites* 41(12), 5285-5296. https://doi.org/10.1002/pc.25774

Liu, X., Liu, Y., Li, Z., Zhao, Q., Zhong, B., Feng, Y., Yu, Y. (2022). "Cellulose nanofiber reinforced poly(lactic acid) with enhanced rheology for 3D printing,"

Carbohydrate Polymers 287, article 119333. https://doi.org/10.1016/j.carbpol.2022.119333

Lozano Fernandez, M. E., and Miskolczi, N. (2022). "Production of cellulose nanofibers and its application in poly-lactic-acid: Property improvement by new types of coupling agents," *Polymers* 14(9), 1887-1899. https://doi.org/10.3390/polym14091887

Lu, Y., Luo, Q., Jia, X., Lan, D., Li, Y., Liu, F., Leng, Y., Huang, D., Du, S., and Wei, D. (2022). "Lignocellulose nanofiber/polylactic acid (LCNF/PLA) composite with enhanced mechanical properties and excellent thermal stability prepared by internal mixing and 3D printing," *Industrial Crops and Products* 177, article 114469. https://doi.org/10.1016/j.indcrop.2022.114469

Magee, E., Tang, F., Walker, M., Zak, A., Tenne, R., and McNally, T. (2023). "Silane functionalization of WS_2 nanotubes for interaction with poly(lactic acid)," *Nanoscale* 15(12), 5632-5643. https://doi.org/10.1039/D3NR00583F

Mandal, A., and Chakrabarty, D. (2021). "Characterization of silane-grafted nanocellulose and its effect on PLA composites," *Journal of Applied Polymer Science* 138(20), article e50354. https://doi.org/10.1002/app.50354

Meng, W., Wang, S., Lv, H., Wang, Z., Han, X., Zhou, Z., and Pu, J. (2022). "Porous cellulose nanofiber (CNF)-based aerogel with the loading of zeolitic imidazolate frameworks-8 (ZIF-8) for Cu(II) removal from wastewater," *BioResources* 17(2), 2615-2631. https://doi.org/10.15376/biores.17.2.2615-2631

Mohammed, A. S., Karim, A. A., Bhat, R., Harvinder, S. K., and Min-Tze, L. (2022). "Interfacial bonding mechanisms of natural fibre-matrix composites: An overview," *BioResources* 17(4), 1-45. https://doi.org/10.15376/biores.17.4.Mohammed

Moscoso-Sánchez, F. J., Alvarado, A., Martínez-Chávez, L., Hernández-Montelongo, R., Fernández Escamilla, V. V., and Canche Escamilla, G. (2019). "The effects of henequen cellulose treated with polyethylene glycol on properties of polylactic acid composites," *BioResources* 14(4), 8418-8432. https://doi.org/10.15376/biores.14.2.2707-2726

Nazrin, A., Sapuan, S. M., Zuhri, M. Y. M., Tawakkal, I. S. M. A., Ilyas, R. A. (2021). "Effects of fiber treatments on the mechanical, thermal, and biodegradation properties of sugar palm fiber reinforced PLA biocomposites," *Polymers* 13(16), article 2717. https://doi.org/10.3390/polym13162717

Neves, R. M., Ornaghi, H. L., Zattera, A. J., and Amico, S. C. (2020). "The influence of silane surface modification on microcrystalline cellulose characteristics," *Carbohydrate Polymers* 230, article 115595. https://doi.org/10.1016/j.carbpol.2019.115595

Panaitescu, D. M., Hermida, A. S., Frone, A. N., Gabor, R. A., Nicolae, C. A., Trica, B., Semenescu, A., and Oancea, M. I. (2022). "Poly(lactic acid)/Poly(3-hydroxybutyrate) biocomposites with differently treated green cellulose fibers," *Molecules* 27(8), article 2390. https://doi.org/10.3390/molecules27082390

Piorkowska, E., and Paszkiewicz, S. (2022). "Modification of cellulose micro- and nanomaterials to improve properties of aliphatic polyesters/cellulose composites: A review," *Polymers* 14(7), article 1477. https://doi.org/10.3390/polym14071477

Plackett, D., Løgstrup Andersen, T., Batsberg Pedersen, W., and Nielsen, L. (2010). "Biodegradable composites based on polylactic acid and wheat straw fibres," *Composites Science and Technology* 70(5), 719-725.

Qian, S., Sheng, K., Yu, K., Xu, L., Lopez, C. A. F. (2018). "Improved properties of PLA biocomposites toughened with bamboo cellulose nanowhiskers through silane modification," *Journal of Materials Science* 53(15), 10920-10932. https://doi.org/10.1007/s10853-018-2377-2

Shi, Q., Zhang, K., Wang, Z., Zhang, J., and Sun, J. (2023). "Recent advances in the application of cellulose nanocrystals in the food industry: A review," *Cellulose* 30(17), 10475-10504. https://doi.org/10.1007/s10570-023-05549-2

Shi, S., Han, G., Yuan, M., Zhang, C., Feng, Y., Huang, Y., and Huang, D. (2022). "APTES grafting of cellulose nanofibers for reinforcing PLA: FTIR, XPS, and performance analysis," *Cellulose* 29(5), 2773-2787. https://doi.org/10.1007/s10570-021-04349-y

Shi, W., Wang, L., Xue, X., Xu, X., Zhang, W., and Zhou, W. (2025). "Advances in nanocellulose-based composites for sustainable food packaging," *BioResources* 20(3), 7983-8001. https://doi.org/10.15376/biores.20.3.Shi

Srisawat, K., Prachayawarakorn, J., and Wang, J. (2022). "Properties of poly(lactic acid)/cellulose nanofiber biocomposites: Effect of polymeric plasticizers," *Industrial Crops and Products* 221, article 119342. https://doi.org/10.1016/j.indcrop.2022.119342

Suryanegara, L., Nakagaito, A. N., and Yano, H. (2010). "The effect of crystallization of PLA on the thermal and mechanical properties of microfibrillated cellulose-reinforced PLA composites," *Composites Part A: Applied Science and Manufacturing* 41(10), 1601-1609. https://doi.org/10.1016/j.compscitech.2009.02.022

Tee, Y. B., Talib, R. A., Abdan, K., Chin, N. L., Basha, R. K., and Yunos, K. F. (2013). "Thermally grafting aminosilane onto kenaf-derived cellulose and its influence on the thermal properties of poly(lactic acid) composites," *BioResources* 8(3), 4468-4483. https://doi.org/10.15376/biores.8.3.4468-4483

Thadathil Varghese, J., Cho, K., Raju, R., Farrar, P., Prentice, L., and Prusty, B. G. (2023). "Effect of silane coupling agent and concentration on fracture toughness and water sorption behaviour of fibre-reinforced dental composites," *Dental Materials* 39(4), 362-371. https://doi.org/10.1016/j.dental.2023.03.002

Thomas, P., Hosseini, E., Pfitzner, E., Gurave, P. M., Thomas, S., Pothan, L. A., and Resalati, H. (2021). "Nanocellulose: Extraction from bio-wastes and fabrication of polymer film," *Polymers* 13(11), article 1834. https://doi.org/10.3390/polym13111834

Wang, H., Liu, X., Liu, J., Wu, M., and Huang, Y. (2022). "Tailoring interfacial adhesion between PBAT matrix and PTFE-modified microcrystalline cellulose additive for advanced composites," *Polymers* 14(10), article 1973. https://doi.org/10.3390/polym14101973

Xu, H., Balea, A., Merayo, N., Martínez, A., and Negro, C. (2024). "Improving sustainability of cellulose nanofibrils production: FTIR spectroscopy for online control of the synthesis of recyclable magnetic TEMPO catalyst," *Carbohydrate Polymer Technologies and Applications* 2024, article 100417. https://doi.org/10.1016/j.carpta.2023.100417

Yang, B., Xuan, F., Lei, H., Zhang, Y., Hu, Z., and Liu, G. (2020). "PLA reinforced with APTES-treated microcrystalline cellulose: Influence on Young's modulus and biodegradability," *Materials* 13(22), article 5086. https://doi.org/10.3390/ma13225086

Yu, J., Wang, Y., and Wang, L. (2018). "Manufacturing, mechanical and flame retardant properties of poly(lactic acid) biocomposites based on calcium magnesium phytate and carbon nanotubes," *Composites Part A: Applied Science and Manufacturing* 113, 111-120. https://doi.org/10.1016/j.compositesa.2018.04.027

Yun, Y., Kang, H., Kim, E. C., Park, S., Lee, Y. S., and Yun, K. (2023). "Fundamental properties and clinical application of 3D-printed bioglass porcelain fused to metal dental restoration," *International Journal of Molecular Sciences* 24(8), article 7203. https://doi.org/10.3390/ijms24087203

Zhang, K., Li, Y., Wang, Y., Zhao, J., Chen, L., and Pan, Y. (2023). "Crystallization and thermal behavior of PLA induced by silane-modified cellulose nanofibers," *Cellulose* 30(1), 505-524. https://doi.org/10.1007/s10570-022-04721-z

Zhang, R., Han, B., Liu, L., Zhou, G., Zhang, Q., Wang, K., and Wang, S. (2021). "PLA/bamboo cellulose nanofiber composites: Effect of silane coupling agent dosage on interfacial bonding," *International Journal of Biological Macromolecules* 181, 1124-1135.

Zhang, X., Li, Y., and Wang, Z. (2025). "Role of silane compatibilization on cellulose nanofiber reinforced poly(lactic acid) (PLA) composites with superior mechanical properties, thermal stability, and tunable degradation rates," *Composites Part B: Engineering* 270, article 110927. https://doi.org/10.1016/j.compositesb.2024.110927

Article submitted: October 21, 2025; Peer review completed: November 8, 2025; Revised version received: November 9, 2025; Accepted: November 10, 2025; Published: December 19, 2025.
DOI: 10.15376/biores.21.1.1172-1191